Investigating the Photo and Thermal Stability of Organic Solar Cells with Different Donor–Acceptor Combinations and an ALD-SnOx Interlayer

Professor:

Derya Baran

derya.baran@kaust.edu.sa

Mentor:

Anuj Kumar Singh

anujkumar.singh@kaust.edu.sa

Student:

Daleean Abdulaziz Alkhamees

daleean.alkhamees@kaust.edu.sa

24 / Aug /2026

Table of Contents

Abstract 4
1. Introduction 5
2. Methodology 6
2.1 Materials 6
2.2 Devices fabrication steps 6
2.3 J-V Characterization 7
2.4 UV-Vis-NIR Spectrophotometer absorption 8
2.5 External Quantum Efficiency (EQE) 8
2.6 The Photostability 8
2.7 The thermal stability 9
3. Results and Discussion 10
3.1 Efficiency of photocurrent generated 10
3.2 The EQE test 12
3.3 Photo and thermal stability 13
4. Conclusion and Future Work 15
4.1 Conclusion 15
4.2 Future Work 16
References 17

List of Figures

Figure 1: Schematic diagram of the arrangement of layers of all the devices. 6
Figure 2: J-V curve and the P-V curve[10]. 7
Figure 3: Photostability chamber with the UV filter. 9
Figure 4: The thermal stability setup. 9
Figure 5: The UV-Vis-NIR spectroscopy for all the active layer types. 10
Figure 6: (a) The FF Pmax for the best preforming 5 pixels from each type of active layer blend (b)The Pmax for the best preforming 5 pixels from each type of active layer blend. 11
Figure 7: J-V characterization for the best preforming pixels from each type of active layer. 11
Figure 8: The EQE for all the active layer types. 12
Figure 9:The photostability result for the 4 types of active layers with and without the UV filter. 14
Figure 10: the thermal stability result of the four different types of active layers. 15

List of Tables

Table 1: Active layer combination solutions. 7

Table 2: The Jso,Voc,FF, and the Pmax for the best preforming pixels from each type of active layer. 12

Table 3: Effect of UV filtering on the PCE stability of four OSC systems under continuous illumination. 14

Abstract

This work investigates the photo and thermal stability of inverted organic solar cells (OSCs) fabricated using four donor-acceptor combinations: PM6:Y12, PM6:L8-BO, PCE10:Y12, and PCE-10:L8-BO, integrated with an ALD-SnO_x electron transport layer. Devices were prepared under identical processing conditions and evaluated through UV-Vis-NIR absorption, external quantum efficiency (EQE), J-V characterization, long-term photostability under continuous illumination, and thermal aging at 85 °C. PM6:Y12 exhibited the broadest absorption window and the highest overall EQE response, while PM6:L8-BO demonstrated the strongest initial device performance, achieving the highest maximum power output (Pmax) of 14.9 mW/cm². In contrast, PCE10-based blends generated lower photocurrent but demonstrated superior stability. Photostability tests showed that PM6-based devices degraded rapidly without UV filtering, with PM6:Y12 and PM6:L8-BO retaining only 53% and 43% of their initial performance, respectively, whereas PCE10:Y12 retained approximately 90%. Applying a UV filter significantly improved the stability of all systems, particularly PM6:L8-BO, which increased from 0.43 to 0.70 normalized PCE. Thermal stability measurements further showed that PM6-based devices degraded faster than PCE10-based devices at 85 °C. Overall, the results demonstrate a trade-off between initial device performance and long-term stability and highlight the importance of donor–acceptor selection, UV protection, and control of the ALD-SnO_x interface for improving OSC durability under operational stress.

1. Introduction

Organic solar cells (OSCs) are lightweight, flexible photovoltaic devices built from carbon-based semiconductors, offering tunable optoelectronic properties and low-temperature solution processing suitable for scalable, next-generation solar technologies[1]. Inverted OSCs (i-OSCs) provide superior thermal and moisture stability because their device architecture incorporates a high-work-function silver (Ag) electrode and a metal-oxide electron transport layer (ETL), which improves chemical robustness, prevents ITO corrosion, and enhances resistance to oxygen, humidity, and heat[2], [3].

Among widely used donor polymers, PM6 enables high efficiencies but suffers from significant photodegradation under prolonged illumination, especially UV-rich light, and becomes a weak point in device stability when oxygen is present due to the formation of light-induced traps [4], [5]. In contrast, PCE10 is a low-band-gap donor known for its excellent photostability, retaining most of its efficiency during long-term exposure and showing far fewer light-induced changes compared with PM6 [5].

PCE10 is a widely used low-band-gap polymer donor known for its reliable performance in organic solar cells. Compared with PM6, PCE10 shows much higher stability under illumination-including UV light-because it undergoes far fewer light-induced changes, allowing it to retain most of its efficiency during long-term exposure while PM6 degrades more quickly [5].

The Y-series acceptors L8-BO and Y12 also play a critical role in device stability. L8-BO forms highly ordered domains with low energetic disorder, strong electronic coupling, and efficient electron transport, enabling stable and well-packed donor–acceptor blends[4], [6]. stable Y-series acceptor, with long internal side chains and fluorinated end groups that suppress photodegradation, giving Y12 exceptional photostability and strong outdoor [4].

Metal-oxide ETLs further influence device stability. Although common oxides such as ZnO and TiO_2 suffer from contact barriers, oxygen-vacancy defects, and stability losses, SnO_2 becomes significantly more stable and efficient when its oxygen vacancies are passivated [7]. Atomic Layer Deposition (ALD) produces uniform SnO_x films that avoid oxygen-related damage to the active layer and provide superior UV stability, though remaining oxygen-vacancy defects can still affect charge extraction and must be carefully controlled [8].

Given these considerations, combining stable donor-acceptor systems with a robust ALD-SnO_x interlayer offers a promising route to improving both photo and thermal stability in OSCs. Therefore, this work investigates the stability of OSCs fabricated using four donor-acceptor combinations PM6:Y12, PM6:L8-BO, PCE10:Y12, and PCE10:L8-BO and evaluates how an ALD-SnO_x interlayer influences their photostability and thermal durability under continuous illumination and elevated temperature.

2. Methodology

2.1 Materials

Substrates with the 15-ohm Indium Tin Oxide (ITO)-coated glass, measuring 24.8 mm by 24.8 mm, ALD-SnOx electron transport layer (ETL). Now, for the active layers, the donors that were used are PM6 and PCE-10. And for the acceptor, we used Y12 and L8-BO. The hole transport layer (HTL) was BM-HTL-1. And finally, the metal electrode was silver (Ag).

2.2 Devices fabrication steps

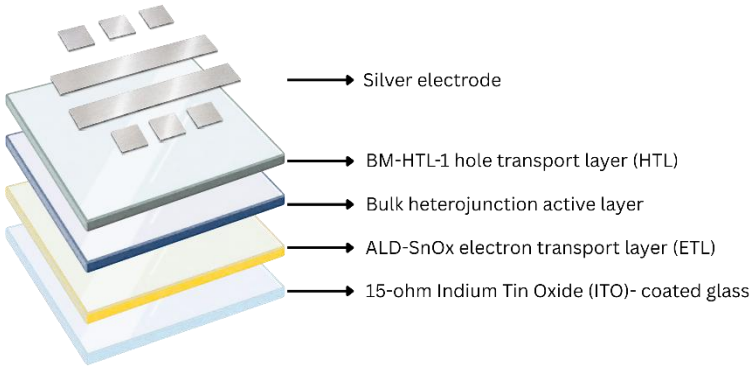


Figure 1: Schematic diagram of the arrangement of layers of all the devices.

First, clean the substrates with the 15-ohm Indium Tin Oxide (ITO)-coated glass, measuring 24.8 mm by 24.8 mm, using soap and water, brushing them gently while cleaning. Rinse them with DI water, then ultrasonicate in a series of DI water, acetone, and isopropyl alcohol (IPA) for 15 min each. Dry them afterwards. The glass with Indium Tin Oxide (ITO) of 15 ohms is used after depositing the ALD-SnOx electron transport layer (ETL). 12 nm SnOx was then deposited on a patterned ITO substrate at 180 °C with a 1.6s TDSMA pulse and a 0.1 water pulse in a Atomic Layer Deposition (ALD) system. SnOx thickness was measured using ellipsometry.

The ratios used to make the bulk heterojunction active layer are listed in Table 1. All the solutions were made in a nitrogen-filled glovebox with no exposure to air; they were mixed at 500 rpm for 45-60 minutes at room temperature. 26 µL of the active layer solution was used for spin coating for all the active layer types. The solution with PM6 was spin-coated on the substrate at a speed of 3000 rpm for 15-20 seconds, while the ones with PCE-10 used a speed of 2600 rpm for 15-20 seconds; both were annealed for 1 minute at 95°C, then spin-coated with 70 µL of the BM-HTL-1 (HTL) at 3000 rpm with no annealing afterwards.

Then the devices were moved to the thermal evaporator to deposit a layer of silver as the metal electrode with a thickness of 100nm.

Table 1: Active layer combination solutions.

Donor	Acceptor	Solvent	Ratio with respect to donor	Concentration with respect to donor
PM6	Y12	Chloroform (CF)	1:1.25	7.5 mg/mL
PM6	L8BO	Chloroform (CF)	1:1.25	7.5 mg/mL
PCE-10	Y12	Chloroform (CF)	1:1.25	7.2 mg/mL
PCE-10	L8BO	Chloroform (CF)	1:1.25	7.2 mg/mL

2.3 J-V Characterization

All devices were characterized using J-V to obtain the short-circuit current density (J_{sc}), open-circuit voltage (V_{oc}), fill factor (FF), and power conversion efficiency (PCE). The maximum power point (MPP) was determined from the J-V curve by calculating the electrical power at each voltage using $P = J \times V$. The corresponding V_{MPP} and J_{MPP} values were then used to compute the fill factor:

$$FF = \frac{V_{MPP} \times J_{MPP}}{V_{oc} \times J_{sc}}$$

The power conversion efficiency was calculated as:

$$PCE = \frac{P_{MPP}}{P_{sun}} = \frac{V_{MPP} \times J_{MPP}}{P_{sun}}$$

The active area of each device was 0.1 cm². J–V scans were performed from –0.2 V to 1.0 V with a step size f 0.05 V, and the current compliance was set to 0.2 A.

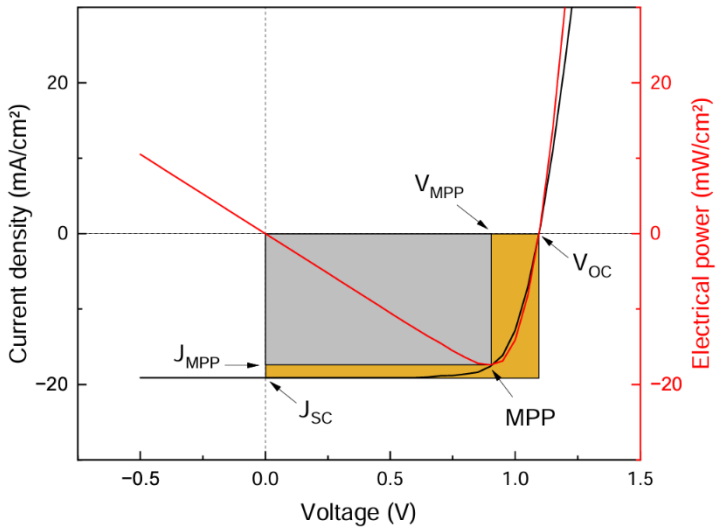


Figure 2: J-V curve and the P-V curve[10].

2.4 UV-Vis-NIR Spectrophotometer absorption

UV-Vis-NIR spectroscopy was used to evaluate the optical absorption characteristics of the donor-acceptor materials. Measurements were performed using a UV-Vis-NIR spectrophotometer operating in the 300-1050 nm range. Thin films were deposited on glass substrates under identical spin-coating conditions (2500 rpm, 35 µL per solution). A bare glass ITO served as the reference for baseline correction.

As light passes through the sample, the transmitted intensity decreases when the photon energy matches available electronic states, indicating absorption. The resulting spectra reveal the absorption and transmittance behaviour of each donor-acceptor system across the measured wavelengths. These data allow us to determine the optical absorption range of each active-layer combination.

2.5 External Quantum Efficiency (EQE)

External Quantum Efficiency (EQE) measurements were performed to determine the wavelength-dependent photocurrent generation of the organic solar cells. The EQE setup consisted of a calibrated broadband light source coupled to a monochromator that provides narrowband illumination across the 300-1000 nm range. The device was held under short-circuit conditions while the modulated monochromatic light illuminated the active area.

The photocurrent generated at each wavelength, $J_{ph}(\lambda)$, was normalized to the incident photon flux measured using a calibrated silicon photodiode. The EQE was calculated using:

$$EQE = \frac{collected\ charge\ carriers}{incident\ photons}\ or\ \frac{J_{ph}(\lambda)}{q\phi_{ph}(\lambda)}$$

where q is the elementary charge and $\phi_{ph}(\lambda)$is the spectral photon flux. The resulting EQE spectrum reveals how efficiently the device converts incident photons into collected charge carriers and allows direct comparison with the optical absorption profiles obtained from UV-Vis-NIR spectroscopy.

2.6 The Photostability

For photostability measurements, the devices were placed inside a metal chamber with nitrogen gs flowing as shown in Figure 3b to prevent the interaction of oxygen and humidity with the devices, and equipped with a water-cooling system, and then exposed to illumination from a 1000 W Solixon A-70-CU-2 plasma lamp. The reading of the J-V is taken by the computer every 10 minutes for 330 hours. A pair of each donor-acceptor combination is placed inside the chamber, covering one of each type with a UV filter on top as shown in Figure 3a.

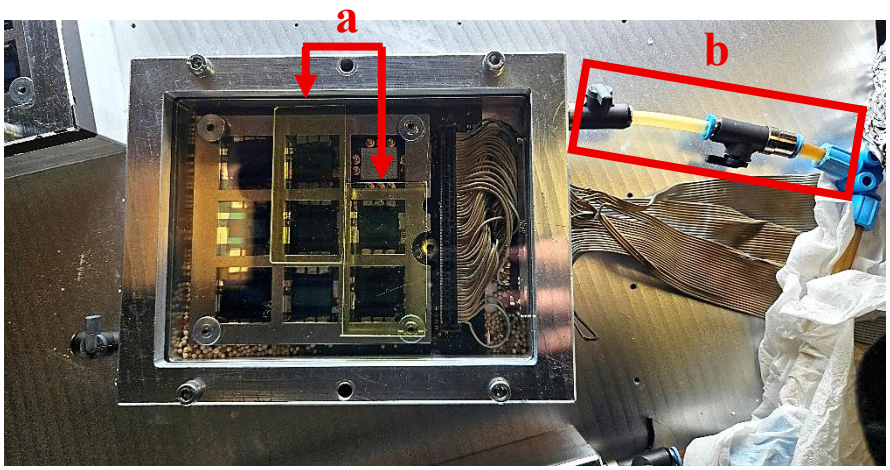


Figure 3: Photostability chamber with the UV filter.

2.7 The thermal stability

Thermal stability was evaluated by placing the four types of donor-acceptor blends OSC inside a nitrogen glove box on a hot plate set to 85°C as in the Figure 4a. A large glass petri dish covered with aluminium foil was used to create a controlled heating environment which is shown in the Figure 4b. The four donor-acceptor blends were tested. The samples were heated for the specified duration, cooled inside the glove box, and subsequently characterized using J-V assess thermal degradation.

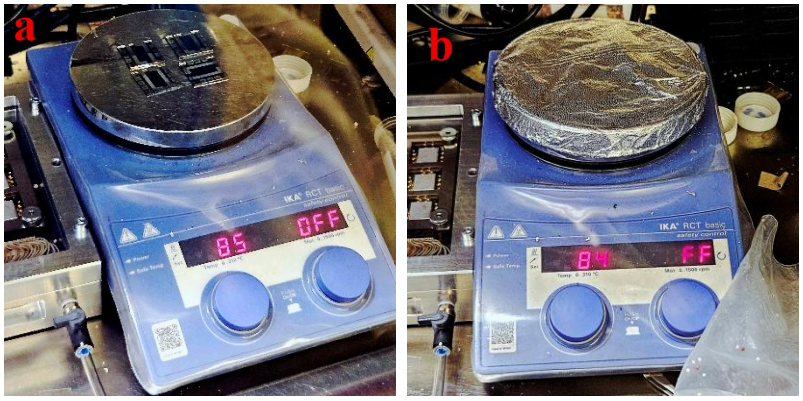


Figure 4: The thermal stability setup.

3. Results and Discussion

3.1 Efficiency of photocurrent generated

The UV-Vis-NIR spectra of the four donor-acceptor combinations in Figure 5 show clear differences in optical absorption across the visible and near-infrared regions. PM6 based blends (PM6:Y12 and PM6:L8-BO) exhibit stronger absorption in the 500-700 nm region, consistent with the broader visible absorption of PM6. In contrast, PCE-10 blends show slightly weaker absorption in this region but maintain a smoother profile across the spectrum. The Y12 acceptors extend absorption toward the near-infrared. As a result, PM6:Y12 demonstrate the broadest absorption windows, indicating better harvesting of low-energy photons.

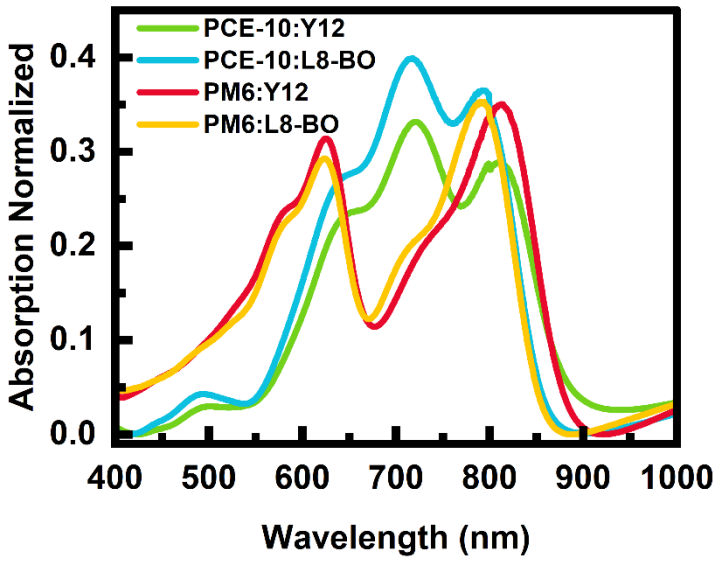


Figure 5: The UV-Vis-NIR spectroscopy for all the active layer types.

We can see in Figure 6 the fill factor (FF) and the maximum power output performance (P_{max}) of the different active layers, as mentioned before PM6:Y12 had the wider range of absorbing in the Vis-NIR regions, but the PM6:L8-BO showed a higher FF and Pmax among all the other combination, on the other hand PCE-10 blends had the weaker FF and P_{max}.

PM6:L8-BO demonstrates the highest and most consistent FF values, suggesting reduced recombination losses and better charge transport within the blend. In contrast, PCE-10:Y12 and PCE-10:L8-BO show a lower median values of FF.

The maximum power output (P_{max}) in Figure 6b follows the same trend. PM6:L8-BO achieves the highest Pmax among all active-layer combinations, while the PM6:Y12 shows moderate P_{max} values, and both PCE-10 blends exhibit significantly lower and broader variation

performance. These results confirm that PM6 paired with L8-BO provides the most efficient combination of optical absorption, charge generation, and charge transport, leading to the strongest overall device performance.

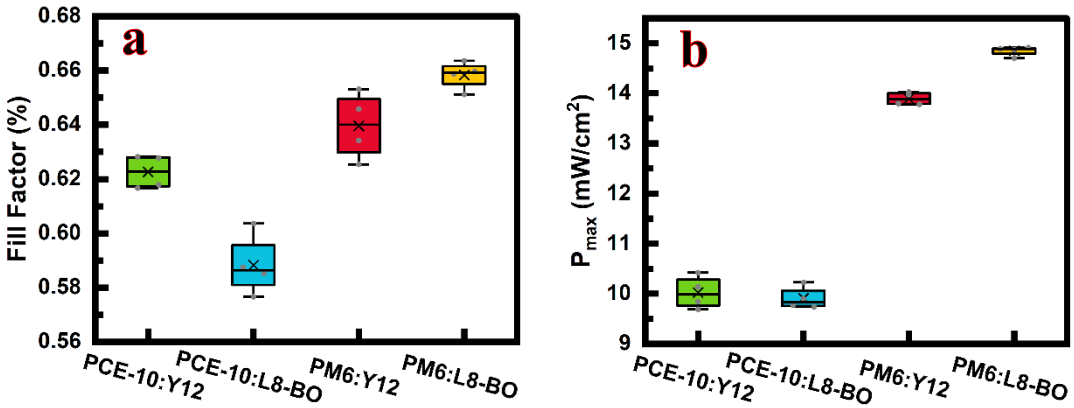


Figure 6: (a) The FF Pmax for the best preforming 5 pixels from each type of active layer blend (b)The Pmax for the best preforming 5 pixels from each type of active layer blend.

The J-V characteristics of the best performing pixels as shown in Table 2 reveal the clear differences between the four donor-acceptor systems. PM6-based blends (PM6:Y12 and PM6:L8-BO) show higher short-circuit current densities compared to the PCE-10 blends, consistent with their stronger absorption response in the visible and near-infrared regions. Among all devices, PM6:Y12 exhibits the highest J_{sc} this is consistent with the outcome of the EQE in Figure 8, but the PM6:L8-BO has higher V_{oc} because of its larger band gap as compared to Y12, This balances out overall PCE and FF.

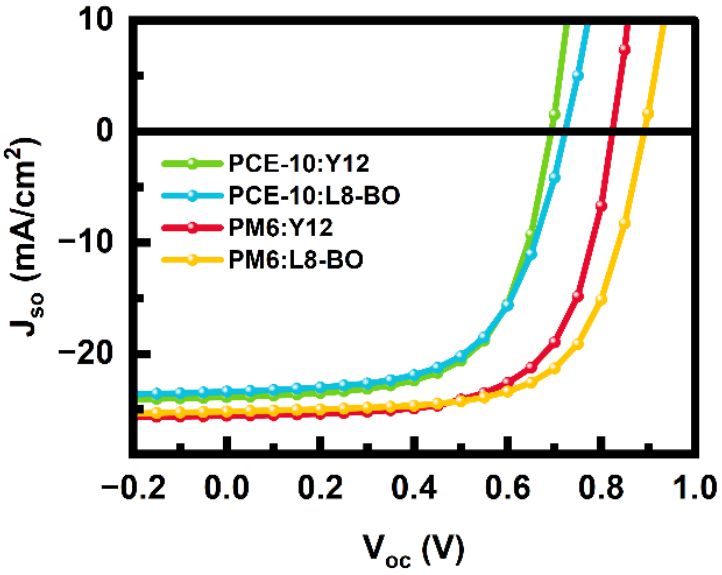


Figure 7: J-V characterization for the best preforming pixels from each type of active layer.

Table 2: The Jso,Voc,FF, and the Pmax for the best preforming pixels from each type of active layer.

	J_{sc}	V_{oc}	FF	P_{max}
PCE-10:Y12	23.894	0.6941	0.6282	10.419
PCE-10:L8-BO	23.396	0.7241	0.6036	10.227
PM6:Y12	26.373	0.8387	0.6342	14.027
PM6:L8-BO	25.175	0.8927	0.6636	14.912

3.2 The EQE test

The EQE spectra follow the same trend observed in the UV-Vis-NIR data. PM6:Y12 shows the highest overall EQE response across the visible and NIR regions, while PM6:L8-BO also exhibits relatively high EQE. PCE-10 blends show lower overall EQE values, consistent with their weaker absorption intensity. The close alignment between the UV-Vis-NIR absorption peaks and the EQE features indicates effective exciton dissociation and charge collection in the PM6-based devices.

Overall, the combined UV-Vis-NIR and EQE results demonstrate that PM6:L8-BO provides a balance between the optical and electronic response, with broad absorption than the PCE-blends and relatively high EQE and great J-V result. This suggests stronger donor-acceptor interaction, more efficient charge generation, and better utilization of near-infrared photons compared to the other blend systems.

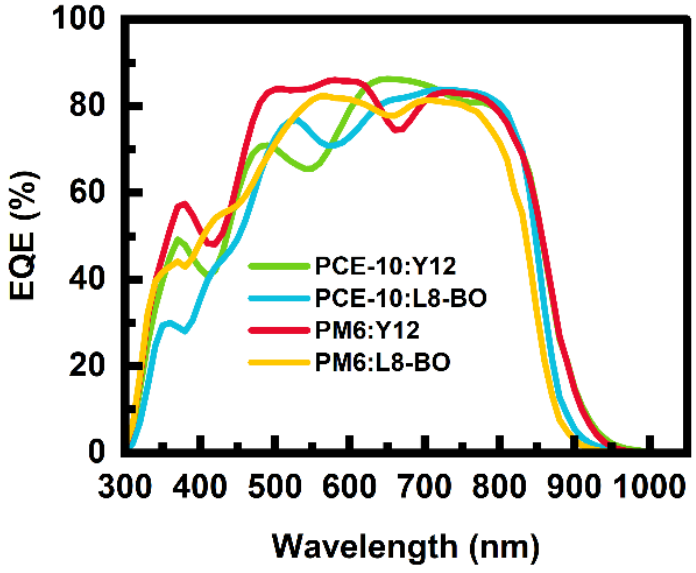


Figure 8: The EQE for all the active layer types.

3.3 Photo and thermal stability

In previous studies, PCE-10 was shown to exhibit superior photostability compared to PM6[5]. and this trend is clearly reflected in Figure 7, under full illumination without a UV filter, the PCE-10:Y12 blend loses only ~ 10% of its initial efficiency, whereas the PM6:Y12 blend suffers a much more severe degradation of ~ 47%, confirming the higher resistance of PCE-10 donor to UV light.

The photostability results in Figure 9 show that all four active layers degrade under continuous illumination, but the UV filter consistently slows this degradation. PCE-10:Y12 and PCE-10:L8-BO show moderate improvement when the UV filter is applied, while the PM6mbased blends are much more sensitive to UV exposure. PM6:Y12 and PM6:L8-BO lose performance quickly without the filter. Overall, the UV filter provides the strongest stabilization for PM6:L8-BO, followed by PM6:Y12, indicating that PM6-based systems benefit the most from UV protection.

In a previous paper, they used the same PM6:L8-BO active layer and the same ALD-SnO_2 ETL as our device-despite having a different HTL-and their stability results match ours, with the PCE dropping to about 70% after ~50 hours of illumination without a UV filter[8]. This means that the HTL has minimal influence on UV-induced degradation compared to the ETL, because the stability behaviour is dominated by the ALD-SnO_2 / active-layer interface.

In another paper they mentioned in their supplemental information that they used the same active layer (PM6:Y12) as ours but with different ETL and HTL, and their devices remained stable for nearly 1000 hours while ours dropped to ~80% after 50 hours, indicating that the ALD-SnO_x interlayer in our structure strongly influences the active layer and confirming that a UV filter can reduce the impact of oxygen-vacancy defects in ALD-SnO_x [4].

The data in Table 3 shows all eight devices' final PCE Normalized achieved over the 330 hours under the illumination with and without the UV filter. The PCE-10:Y12 had the lowest change in the ΔPCE with 0.07 in difference, we can estimate that PM6-based devices suffer the strongest UV-induced degradation, and the large stability improvement with a UV filter indicates that oxygen-vacancy defects in ALD-SnO_x play a major role in this degradation pathway.

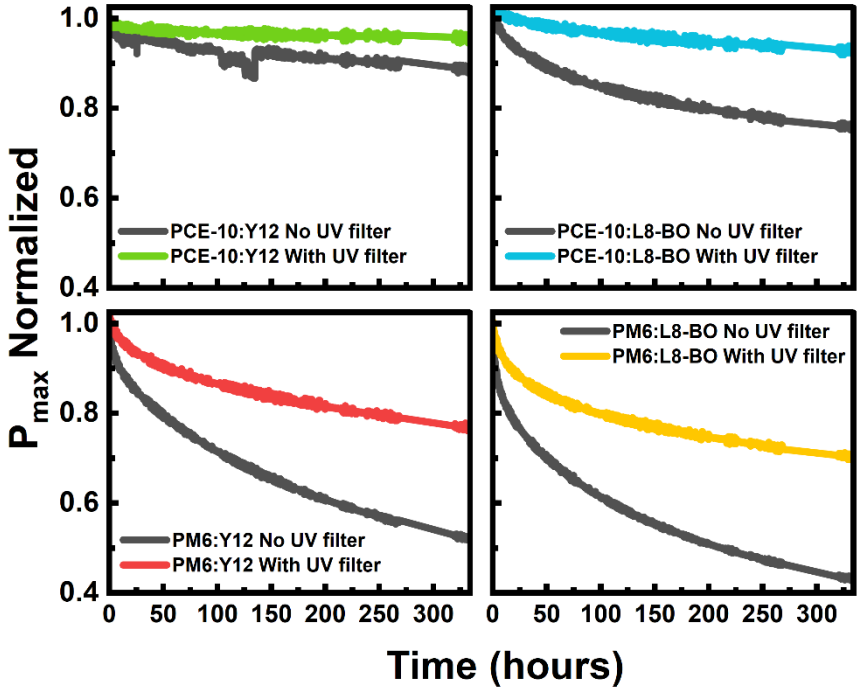


Figure 9:The photostability result for the 4 types of active layers with and without the UV filter.

Table 3: Effect of UV filtering on the PCE stability of four OSC systems under continuous illumination.

	Last normalized PCE for the devices with no UV filter	Last normalized PCE for the devices with UV filter	Stability improvement (ΔPCE)
PCE-10:Y12	0.90	0.97	~ 0.07
PCE-10:L8-BO	0.77	0.94	~ 0.17
PM6:Y12	0.53	0.78	~ 0.25
PM6:L8-BO	0.43	0.70	~ 0.27

Under thermal stress at 85 °C, all four donor-acceptor systems exhibited a gradual decline in normalized Pmax, but the PM6-based blends (PM6:Y12 and PM6:L8-BO) degraded significantly faster than the PCE10-based blends, with PM6:L8-BO showing the lowest thermal stability. This behaviour aligns with the fact that most organic semiconductors used in OSCs have glass-transition temperatures (Tg) between 70-90 °C, where the bulk-heterojunction (BHJ) morphology begins to relax, reorganize, and lose optimal phase separation, leading to reduced charge transport and accelerated performance loss [9]. In contrast, PCE10-based devices maintained higher stability throughout the 400-hour heating period, indicating a more thermally robust morphology and weaker sensitivity to interfacial

defects at the ALD-SnOx interface. Improving thermal durability will require designing high-Tg donor and acceptor materials or incorporating thermoset-based BHJ systems that lock the morphology in place, a strategy recently demonstrated to enhance long-term stability under elevated temperatures [9].

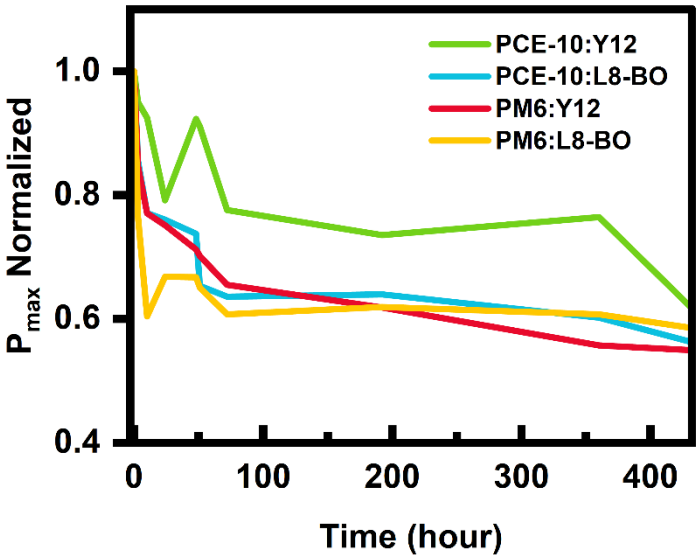


Figure 10: the thermal stability result of the four different types of active layers.

4. Conclusion and Future Work

4.1 Conclusion

This work investigated the performance, photostability, and thermal stability of inverted organic solar cells based on four donor–acceptor combinations: PM6:Y12, PM6:L8-BO, PCE10:Y12, and PCE10:L8-BO, using ALD-SnO_x as the electron transport layer. The results demonstrate a clear trade-off between initial device performance and long-term stability.

Among the investigated systems, PM6:L8-BO exhibited the strongest initial device performance, achieving the highest maximum power output and fill factor. In contrast, the PCE10-based devices showed lower initial performance but significantly better stability. PCE10:Y12 demonstrated the highest photostability, retaining approximately 90% of its initial performance after 330 hours of continuous illumination without UV filtering and approximately 97% when a UV filter was applied.

The use of a UV filter improved the photostability of all four systems, with the largest improvement observed for PM6:L8-BO and PM6:Y12. This indicates that UV exposure plays an important role in the degradation of PM6-based devices. The thermal stability measurements at 85 °C showed a similar trend, with PCE10-based devices exhibiting greater resistance to thermal degradation than PM6-based devices.

Overall, the results highlight that achieving highly durable organic solar cells requires balancing high initial efficiency with long-term stability. While PM6:L8-BO provided the best initial performance, PCE10:Y12 offered the most promising stability. The significant improvement obtained through UV filtering also demonstrates the importance of controlling UV-induced degradation in devices incorporating ALD-SnO_x interfaces.

4.2 Future Work

Future work should focus on identifying the mechanisms responsible for the degradation observed in these devices and improving the stability of the ALD-SnO_x/active-layer interface. Further investigation of oxygen-vacancy defects in ALD-SnO_x could help determine their contribution to UV-induced degradation.

The ALD deposition conditions, including SnO_x thickness and deposition parameters, could also be systematically optimized to determine their influence on device efficiency and stability. Comparing ALD-SnO_x with alternative electron transport layers would provide further insight into whether the observed degradation originates mainly from the active-layer materials or from interfacial effects.

Longer-term photo and thermal stability measurements should also be performed to determine device lifetimes and compare the different donor–acceptor systems over extended operating periods. Finally, investigating high-glass-transition-temperature materials, morphology-stabilization approaches, and improved UV-protection strategies could provide promising routes toward organic solar cells that combine high initial performance with improved long-term operational stability.

References

[1] E. Antolin, J. Urieta-Mora, A. Molina-Ontoria, and N. Martín, "Organic solar cells: Principles, materials, and working mechanism," Apr. 01, 2025, *Elsevier Ltd*. doi: 10.1016/j.cocis.2024.101893.

[2] C. H. Hsieh *et al.*, "Highly efficient and stable inverted polymer solar cells integrated with a cross-linked fullerene material as an interlayer," *J. Am. Chem. Soc.*, vol. 132, no. 13, pp. 4887–4893, Apr. 2010, doi: 10.1021/ja100236b.

[3] Y. Qiu, R. Peng, J. Shi, Z. Chen, and Z. Ge, "Revealing and Eliminating the Light-Soaking Issue in Metal Oxide-Based Inverted Organic Solar Cells," *Adv. Funct. Mater.*, vol. 33, no. 28, Jul. 2023, doi: 10.1002/adfm.202300831.

[4] H. Xu *et al.*, "Dissecting the structure-stability relationship of Y-series electron acceptors for real-world solar cell applications," *Joule*, vol. 7, no. 9, pp. 2135–2151, Sep. 2023, doi: 10.1016/j.joule.2023.07.003.

[5] H. Xu *et al.*, "Elucidating the photodegradation pathways of polymer donors for organic solar cells with seven months of outdoor operational stability," *Nat. Photonics*, vol. 19, no. 4, pp. 415–425, Apr. 2025, doi: 10.1038/s41566-025-01644-x.

[6] Z. Wen, R. Zhou, Z. Zheng, and Y. Zhao, "PM6/L8-BO Thin Films through Layer-by-Layer Engineering: Formation Mechanism, Energetic Disorder, and Carrier Mobility," *Aggregate*, vol. 6, no. 4, Apr. 2025, doi: 10.1002/agt2.729.

[7] R. Yu *et al.*, "Efficient interface modification via multi-site coordination for improved efficiency and stability in organic solar cells," *Energy Environ. Sci.*, vol. 15, no. 2, pp. 822–829, Feb. 2022, doi: 10.1039/d1ee03263a.

[8] L. Di Mario *et al.*, "Outstanding Fill Factor in Inverted Organic Solar Cells with SnO2 by Atomic Layer Deposition," *Advanced Materials*, vol. 36, no. 20, May 2024, doi: 10.1002/adma.202301404.

[9] J. Han *et al.*, "In situ formation of thermoset matrices for improved stability in organic photovoltaics," *Joule*, vol. 8, no. 10, pp. 2883–2902, Oct. 2024, doi: 10.1016/j.joule.2024.07.008.

[10] BSc. Stefan Moser, "Measurement techniques for the external quantum efficiency of perovskite and organic solar cells," *JOHANNES KEPLER UNIVERSITÄT LINZ*, Feb. 2025.